Green Chemistry

PAPER

View Article Online
View Journal | View Issue



Cite this: *Green Chem.*, 2022, **24**, 5620

# Ionically conducting inorganic binders: a paradigm shift in electrochemical energy storage†

Shivam Trivedi, ‡[a] Venkat Pamidi,‡[a] Maximilian Fichtner [a,b] and M. Anji Reddy *[c]

Received 11th April 2022,
Accepted 17th June 2022

DOI: 10.1039/d2gc01389d

rsc.li/greenchem

Among the key components in batteries, binders play a vital role by interconnecting active materials and conductive additives and facilitating the coating of electrode materials on the desired substrates thus enabling the flexible fabrication of batteries. Further, they aid in buffering volume changes that arise in electrode materials and enhance their cycling stability. Presently, polyvinylidene fluoride-based binders are employed widely, despite their high cost, non-eco-friendliness, and energy inefficiency. Several water processable binders have been investigated as alternatives, but they suffer from various intrinsic issues. Here, we reveal the potential of several ionically conducting inorganic binders (ICIBs). These ICIBs are not only ionically conducting, but also water processable, chemically compatible, eco-friendly, low-cost, thermally stable (>1000 °C), emission-free, and importantly, safe to use. These inorganic binders outperformed standard polyvinylidene fluoride-based binders in several aspects. Surprisingly, ICIBs are absorbing the exothermic heat evolved by charged cathode materials at high temperatures, which will significantly enhance the safety of the batteries. The unique intrinsic ionic conductive properties combined with binding abilities enabled the flexible processing and functioning of solid-state batteries, otherwise challenging due to the mechanical rigidity, chemical incompatibility, and interfacial issues posed by solid electrolytes. The inorganic binders introduced here will make battery manufacturing and recycling more energy-efficient, eco-friendly, flexible, safe, and above all, cost-effective.



## Introduction

Polyvinylidene fluoride (PVDF) and its derivatives are employed as binders in the construction of state-of-the-art lithium-ion batteries (LIBs). It has excellent binding characteristics, high chemical and electrochemical stability, good mechanical properties, and is compatible with a wide range of electrode materials.[1] However, PVDF is relatively expensive and produces hazardous HF and fluorocarbons upon decomposition.[2,3] Further, PVDF-based binders demand *N*-methyl pyrrolidone (NMP) for slurry formation and processing. NMP is a toxic,[4,5] high boiling solvent, and high temperature, and thereby, high energy is necessary to remove the NMP from coating.[6] Further, in the recycling of LIBs, PVDF has to burn off for its removal, which is not environmentally benign, contaminates final waste streams, and decreases the value of products.[7] Several eco-friendly and water processable binders have been reported as alternatives to PVDF; among them, sodium carboxymethyl cellulose (NaCMC), sodium polyacrylate (NaPAA), and sodium alginate (NaALG) are in wide use.[8–10] NaCMC is used in commercial applications as a binder for graphite.[11,12] It is aqueous processable and eco-friendly, but it has low thermal stability and produces gaseous species during decomposition (Fig. S1†).

Beyond binding properties, ionic conductivity (IC) within the binder is mandatory to shuttle ions between electrolyte and electrode particles.[13,14] Ionic conductivity in binders is currently induced by injecting liquid electrolytes (LEs). LEs will wet the binders, infuse ionic conductivity and make the battery operational. Nevertheless, the following advantages can be realized if binders possess intrinsic ionic conductivity. Firstly, it will improve the power density of electrodes due to increased charge carrier density and, secondly, enhance the transport number of cations. Ionic transport becomes possible even if liquid electrolyte fails to wet the binder (Ex: high viscous LEs like ionic liquids). This further enables the use of an optimum amount of LE and the design of thicker electrodes, leading to enhanced areal capacity. Batteries can operate

[a]*Helmholtz Institute Ulm (HIU) Electrochemical Energy Storage, Helmholtzstraße 11, 89081 Ulm, Germany*
[b]*Institute of Nanotechnology, Karlsruhe Institute of Technology, PO. Box 3640, D-76021 Karlsruhe, Germany*
[c]*Faculty of Science and Engineering, Swansea University, Fabian Way, Swansea SA1 8EN, UK. E-mail: a.r.munnangi@swansea.ac.uk*
†Electronic supplementary information (ESI) available. See DOI: https://doi.org/10.1039/d2gc01389d
‡These authors contributed equally to this work.

even if LEs would dry out (in conversion electrodes, continuous consumption of LEs from solid electrolyte interphase (SEI) is inevitable, which leads to drying out after a few cycles).[15] Consequently, wetting electrodes in solid-state batteries (SSBs) with LEs is no longer obligatory for SSBs to function if the binder possesses intrinsic ionic conductivity. Though a few reports speculate LiCMC and LiPAA binders are ionically conductive, no evidence was provided towards this.[16–18] Rather, NaCMC was found to conduct protons ($H^+$).[19,20] To verify this assumption, we measured the ionic conductivity of NaCMC, NaPAA, and NaALG (Fig. S2†). Our experiments also led to the conclusion that these binders might conduct $H^+$ rather than $Na^+$. $H^+$ conductivity might not offer the advantages of having intrinsic ionic conductivity discussed above.

Eventually, advanced multifunctional binders are required to meet the future ever-expanding energy demands.[21] To this end, here we reveal the potential of ionically conducting inorganic binders (ICIBs) with multi potentialities to overcome the challenges posed by non-aqueous and solid-state batteries. Lithium salt like $Li_2Si_5O_{11}$ has been known to industries since 1996 for its binding abilities with graphite electrode materials.[22] Later, phosphates and silicates of sodium and lithium were studied as a binder with carbon-based nanocomposite anodes and $LiFePO_4$/C, $LiMnPO_4$/C cathodes for almost a decade ago.[23] Undisputedly, these patents discussed the binding abilities of these inorganic salts without any elaborate discussion on binder properties or electrochemical performance. There was no follow-up work up to now when we came across a recent paper while finalizing this manuscript. In this report, they studied a few inorganic compounds as binders for silicon and graphite anodes in LIBs.[24] This study is technically limited to showcasing the binding abilities of these binders with few electrode materials. Also, no insight into the structure, ionic conductivity, and thermal properties of these binders was provided. Through this study, we reveal the potential of several ionically conducting inorganic binders (ICIB). We have reported twelve ICIBs in this article. The versatility and compatibility of these binders were tested against six different classes of electrode materials and in three battery technologies (lithium-ion, sodium-ion, and solid-state batteries). In all cases, we have compared the performance of ICIB with standard PVDF. We have not only reported the properties of ICIBs but provided deep insight into the structure, ionic conducting mechanisms, thermal properties, and binding properties of these binders.

The twelve inorganic binders investigated in this study are: sodium trimetaphosphate ($(NaPO_3)_3$-STMP), sodium hexametaphosphate ($(NaPO_3)_6$-SHMP), sodium polyphosphate ($(NaPO_3)_n$-SPP), sodium metasilicate ($Na_2SiO_3$-SMS), their 1 : 1 mixture (SPP–STMP; SPP–SHMP; SHMP–STMP; SPP–SMS), sodium hydrogen pyrophosphate ($Na_2H_2P_2O_7$-NHPYO, Fig. S11†), lithium hydrogen phosphate ($LiH_2PO_4$-LHPO), lithium polyphosphate ($LiPO_3$-LPO) and lithium polysilicate ($Li_2Si_5O_{11}$-LPS). Six different classes of electrode materials were (cathode materials: $Na_{0.7}Mn_{0.9}Mg_{0.1}O_2$, $Na_3V_2(PO_4)_3$, $LiMn_2O_4$; anode materials: hard carbon, graphite, $Li_4Ti_5O_{12}$) were examined to study the flexibility of ICIB. All Na-based binders were tested for sodium-ion batteries (SIBs), and Li-based binders were tested for LIBs. Additionally, Na-based SHMP was also tested for LIBs to validate its applicability in LIBs. A comparison of the electrochemical performance of ICIBs was made with that of standard PVDF. We have also compared the electrochemical performance of hard carbon with that of NaCMC and NaALG.

## Structure, thermal properties, and ionic conductivity of ICIB

Among sodium phosphates, only as-received STMP exhibited a crystalline XRD pattern, while SHMP and SPP were in amorphous form (Fig. S3†). Apparently, the crystal structure of STMP alone was reported.[25] The structure of STMP ($Na_3P_3O_9$) is built up of an isolated $(P_3O_9)^{3-}$ cluster network connected three-dimensionally (3D) through $NaO_5$ polyhedra (Fig. 1g). STMP consists of two different Na atoms: Na1 and Na2; both of them are five-fold coordinated to oxygen atoms. $Na1O_5$ polyhedra are connected through a common edge along the *c*-axis. The distance between the Na1 atoms along the *c*-axis is 3.914 Å. The $Na2O_5$ polyhedra are connected through corner-sharing oxygen atoms along *a*-axis; the distance between Na2 atoms is 3.417 Å. $Na2O_5$ polyhedra are diagonally organized with respect to $Na1O_5$. The distance between Na1 and Na2 atoms is 3.576 Å. Though $Na1O_5$ polyhedra are not connected directly along the *a*-axis, they are connected diagonally to $Na2O_5$ through a common edge, generating a zig-zag pathway for $Na^+$ diffusion along the *a*-axis. This distinct inter and intra connection of $Na1O_5$ and $Na2O_5$ polyhedra provides 3D paths for $Na^+$ diffusion in STMP.

Though amorphous at RT, we attempted to investigate the structure of SHMP and SPP. Both remain amorphous even after heating at 200 °C (Fig. 1a); however, SPP crystalized after heating at 300 °C. Its XRD pattern perfectly matches that of STMP and persists even after heating at 600 °C. SHMP also showed a few crystalline peaks after heating at 300 °C, which matches with the XRD pattern of STMP; a few additional peaks were found corresponding to $Na_5P_3O_{10}$. SHMP crystallized completely after heating at 600 °C and converted to STMP (Fig. S3†). The FTIR spectra of STMP were compared with that of $M(NH_4)_4(P_3O_9)_2{\cdot}4H_2O$[26] as its structure is built of isolated $(P_3O_9)^{3-}$ clusters similar to STMP. The peaks at 1294 $cm^{-1}$ and 1262 $cm^{-1}$ correspond to asymmetric stretching vibrations ($\nu_{as}$) of O–P–O (Fig. 1b). The double peaks observed at 1099 $cm^{-1}$ and 1162 $cm^{-1}$ correspond to symmetric stretching vibration ($\nu_s$) of O–P–O. A strong peak at 978 $cm^{-1}$ designates asymmetric stretching vibration of ($\nu_{as}$) of P–O–P. The peaks at 687 $cm^{-1}$ and 753 $cm^{-1}$ confirm symmetric stretching ($\nu_s$) of P–O–P.

The peaks at 513 $cm^{-1}$ and 639 $cm^{-1}$ correspond to deformation vibrations of P–O–P. The peaks at 1255 $cm^{-1}$ and 1085 $cm^{-1}$ designate asymmetric ($\nu_{as}$) and symmetric stretching vibration ($\nu_s$) of O–P–O. These two peaks are red-shifted by

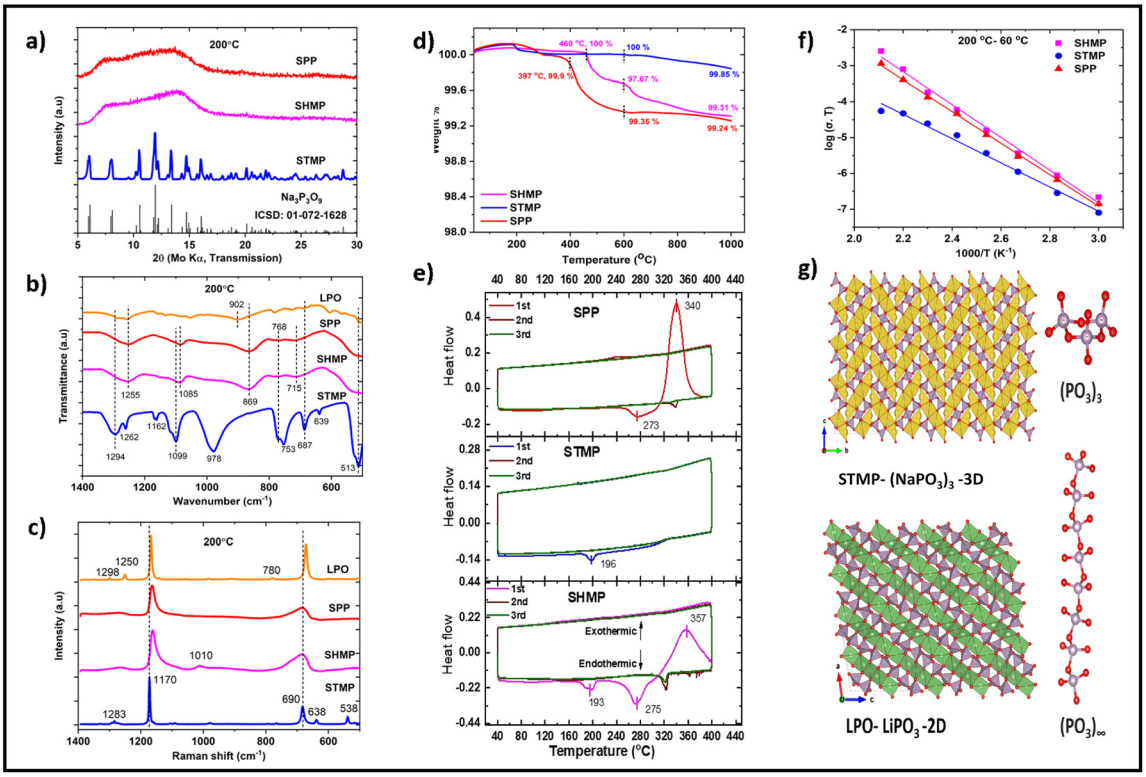


**Fig. 1** Structure, ionic conductivity, and thermal properties of ICIB. (a) XRD patterns of STMP, SHMP, and SPP after heating at 200 °C for 2 h; (b) FT-IR and (c) Raman spectra of crystalline STMP, amorphous SHMP, SPP, and LPO; (d) thermogravimetric analysis (TGA) and (e) differential scanning calorimetry (DSC) of as received STMP, SHMP, and SPP; (f) Arrhenius plot for the IC of crystalline STMP, amorphous SHMP, and SPP; the ionic conductivity of samples was measured after heating the cold-pressed samples at 200 °C for 2 h. The ICs were measured for $T$ = 200–60 °C (top-down with 20 °C intervals); (g) crystal structure view of STMP and $LiPO_3$ (images created by Vesta). Apart from pure sodium phosphates and silicates, we have investigated the ICs and binding properties of a 1 : 1 mixture of STMP, SHMP, and SMS with SPP to explore the existence of synergetic effects. The ICs of these mixed binders are: 6.2 × $10^{-10}$ S $cm^{-1}$ (SHMP: STMP), 3.5 × $10^{-10}$ S $cm^{-1}$ (SHMP: SPP), 1.7 × $10^{-10}$ S $cm^{-1}$ (STMP: SPP) and 5.8 × $10^{-10}$ S $cm^{-1}$ (SMS: SPP) at 60 °C. The ICs are in the same range as in the case with amorphous SHMP and SPP but exhibited superior electrochemical properties compared to pure binders. We have also investigated the ICs, thermal, and binding properties of Li-based ICIB, LHPO, LPO, LPS; however, due to space limitation, the discussion related to these binders are placed in ESI (Fig. S9, S10 and Table S1†).

39 $cm^{-1}$ and 14 $cm^{-1}$ compared to STMP, which indicates an increase in bond length of O–P–O in SHMP and SPP compared to STMP. The strong peak found in STMP at 978 $cm^{-1}$ is absent in SHMP and SPP; however, a new peak evolved at 869 $cm^{-1}$. The peaks at 753 $cm^{-1}$ and 687 $cm^{-1}$ in STMP correspond to P–O–P vibrations and are red-shifted by 15 and 28 $cm^{-1}$, respectively, in SHMP and SPP, signifying the shortened bond length P–O–P. Raman spectra of STMP exhibited two strong peaks (Fig. 1c) at 1170 $cm^{-1}$ and 690 $cm^{-1}$, corresponding to symmetric stretching vibrations ($\nu_s$) of O–P–O and P–O–P,[26] respectively. These two peaks also appeared for SHMP and SPP. However, the peak at 1170 $cm^{-1}$ blue-shifted by 10 $cm^{-1}$ than STMP, consistent with the blue-shift observed for symmetric stretching of O–P–O. Beyond 300 °C, both SHMP and SPP converted to STMP. The FTIR results perfectly match with XRD inferences.

Metaphosphates with an O/P ratio of 3 can exhibit two types of structural geometries, chain or cycle; FTIR and Raman fingerprints pilot to differentiate them. The absence of a peak between 750–1000 $cm^{-1}$ in FTIR spectra affirms cyclic geometry, as with cyclic tetraphosphates,[27] while a strong peak observed at 869 $cm^{-1}$ for SHMP and SPP signifies the presence of chain-like $PO_3$. $LiPO_3$ structure is built of $(PO_3)_\infty$ chains and $LiO_4$ tetrahedra (Fig. 1g); hence a strong peak in the vicinity of 869 $cm^{-1}$ is expected. Indeed, $LiPO_3$ exhibits a strong peak at 902 $cm^{-1}$, suggesting that the peak found at 869 $cm^{-1}$ in SHMP and SPP signifies the presence of a chain-like structure of $PO_3$ groups in them (Fig. 1b). Also, the blue shift of O–P–O (shortened bond length) and redshift of P–O–P (enhanced bond length) stretching frequencies indicate a geometrical change in the $PO_3$ group. Besides, chain phosphates hydrolyze readily in water, unlike cyclic phosphates.[28] SHMP, SPP, and STMP were dissolved in water, dried, and heated at various temperatures to validate this postulate. STMP showed a crystalline XRD pattern that typically matches that of pristine STMP (Fig. S4†). SHMP and SPP dried at room temperature (RT) were amorphous. Interestingly, SHMP and SPP heated at 100 °C showed crystalline peaks corresponding to $NaH_2PO_4$ and $Na_2H_2P_2O_7$, the hydrolyzed products of SHMP and SPP. Further, the fraction of $NaH_2PO_4$ is higher than $Na_2H_2P_2O_7$ in

 

SPP at 100 °C. In contrast, the fraction of $Na_2H_2P_2O_7$ is more in SHMP as compared to $NaH_2PO_4$ at 100 °C. This confirms that the chain length of $(PO_3)_\infty$ in SHMP and SPP is different. Shorter chains have a higher fraction of orthophosphate ($NaH_2PO_4$) due to a large fraction of end groups, and longer chains have a large fraction of pyrophosphate ($Na_2H_2P_2O_7$). However, these hydrolyzed phosphates were converted to STMP after heating ≥300 °C. The differences in chemical reactivity of SHMP and SPP compared to STMP confirm the structural differences between these phosphates.

Thermal characteristics of ICIBs were studied using thermogravimetric analysis (TGA) and differential scanning calorimetry (DSC). A weight loss of <1 wt% observed in ICIB (<1000 °C) is attributed to the loss of surface functionalized $OH^-$ in the form of water (Fig. 1d). SPP and SHMP exhibited endothermic regions centered at 273 °C and 275 °C, followed by exothermic peaks centered at 340 °C and 357 °C. The endothermic peaks indicate $T_g$ of SHMP and SPP, while the exothermic peaks signify crystallization (phase transformation to STMP, Fig. 1f). The thermal behavior of SHMP and SPP is consistent with XRD and FT-IR results, supplementing phase transformation in them when heated ≥300 °C. It is inferred that only STMP is stable in the crystalline state (RT–1000 °C) among STMP, SHMP, and SPP. SHMP and SPP are stable in their amorphous state up to 250 °C but become crystalline >250 °C, eventually transforming to STMP. It is concluded that the structure of amorphous SHMP and SPP is composed of $(PO_3)_\infty$ chains, and their local structure is similar to $LiPO_3$ (Fig. 1g). Further, $(PO_3)_\infty$ chain length is distinct for SHMP and SPP. The structural differences in SHMP, SPP, and STMP substantiate the existence of distinct $Na^+$ diffusion paths. The continuously connected $(PO_3)_\infty$ chains in SHMP and SPP (in contrast to isolated $P_3O_9$ groups in STMP) isolate the $NaO_5$ polyhedra in one direction and essentially limit the diffusion to a 2D path (Fig. 1g).

The ionic conductivity of crystalline STMP is $6.1 \times 10^{-11}$ S $cm^{-1}$ at 60 °C that increased to $1.2 \times 10^{-7}$ S $cm^{-1}$ at 200 °C (Fig. 1f). The ionic conductivity increased linearly with the increase in temperature. The activation energy of crystalline STMP was found to be 0.66 eV. The ionic conductivities of amorphous SHMP and SPP were $6.5 \times 10^{-10}$ S $cm^{-1}$ and $4.2 \times 10^{-10}$ S $cm^{-1}$ respectively at 60 °C and increased to $5.3 \times 10^{-6}$ S $cm^{-1}$ and $2.4 \times 10^{-6}$ S $cm^{-1}$ at 200 °C. Corresponding activation energies are 0.89 and 0.87 eV respectively. For comparison, we have synthesized and measured the ionic conductivity of amorphous STMP. Amorphous STMP was made by mechanically milling the crystalline STMP. The ionic conductivity of amorphous STMP was $4.5 \times 10^{-10}$ S $cm^{-1}$ at 60 °C, *i.e.*, ~8 times higher compared to the value of crystalline STMP. The activation energy increased to 0.94 eV from 0.66 eV in amorphous STMP. The ionic conductivities of amorphous phases are 7–10 times higher than crystalline STMP. The enhanced ionic conductivities of amorphous forms are attributed to their different local structures compared to crystalline phosphates (as probed by XRD, FTIR, Raman, and thermal studies). It could also be due to higher defect concentration in amorphous phases, facilitating ion-diffusion and leading to improved ionic conductivity. Interestingly, the activation energy of crystalline STMP is lower than in amorphous phases. Generally, higher ionic conductivities will lead to lower activation energies or vice versa.[29] According to the Anderson-Stuart model, the activation energy for conduction may be the electrostatic binding energy of the original site and the strain energy required to move the ion from one site to another.[30,31] The low activation energy of crystalline STMP indicates the low energy required for ionic movement. If ionic movement is facilitated, higher ionic conductivity can be achieved. Therefore, we postulate that by improving the Na vacancies *via* aliovalent doping, ionic conductivity in crystalline STMP can be improved significantly. Conclusively, the ionic conductivities of ICIB reported here are lower than solid electrolytes (SEs), where the ionic conductivities of SEs are in the range of $10^{-3}$ to $10^{-6}$ S $cm^{-1}$ at RT. It has to be noted that the ionic conductivities reported here are for pure compounds, which will be generally low due to fewer intrinsic defects. Also, there are no apparent vacant sites that could facilitate the $Na^+$ hopping as inferred from crystal structure analysis. The creation of extrinsic defects is necessary to achieve higher ionic conductivity in these binders.

We also measured the ionic conductivity of organic binders NaCMC, NaPAA, and NaALG. For ionic conductivity measurements, the powders were vacuum dried at 120 °C for 12 h. These dried powders were pressed into 7 mm pellets, coated with gold on both sides, and transferred to the glove box, dried further at 100 °C before loading into the EIS cell in the glove box. The ionic conductivities of NaPAA, NaALG are $8.7 \times 10^{-10}$ S $cm^{-1}$ $1.1 \times 10^{-10}$ S $cm^{-1}$ at 60 °C and $2.5 \times 10^{-6}$ S $cm^{-1}$, $1.3 \times 10^{-7}$ S $cm^{-1}$ at 200 °C, respectively. These values are similar to the ionic conductivities of ICIB reported here. In the case of NaCMC, ionic conductivity could not be measured at 60 °C. Its ionic conductivity at 100 °C is $1.1 \times 10^{-10}$ & $1.4 \times 10^{-8}$ at 200 °C. However, the reported $H^+$ conductivity of NaCMC is $3.8 \times 10^{-5}$ S $cm^{-1}$ at RT, much higher than what we measured.[20] In this report, the authors just desiccated the sample before measuring the ionic conductivity. This will not be enough to remove the water from the sample. Our TG analysis showed that these binders absorbed a significant amount of water (~10 wt%) and required heating up to 150 °C to remove the absorbed water (Fig. S1†). $H^+$ transfer occurs through the Grotthus mechanism, and water absorption should enhance $H^+$ conductivity if $H^+$ is the conducting ion. Nafion is another well-known example of hydration-dependent conductivity.[32] To check this, we left the pellets in an atmosphere for 72 h and allowed them to reabsorb the water. The weight of the pellets increased from 77.1 mg to 90.8 mg for NaCMC, 69 mg to 88.2 mg for NaPAA, 67.2 mg to 80.8 mg for NaALG due to the absorption of water. 10 to 20 wt% of weight gain was observed, which is consistent with TG results. We measured the ionic conductivity of these air-exposed samples. Indeed, the ionic conductivity increased to $1.5 \times 10^{-7}$ S $cm^{-1}$ for NaCMC, $7.2 \times 10^{-6}$ for NaPAA, $1.2 \times 10^{-6}$ S $cm^{-1}$ for NaALG at 60 °C, indicating that these compounds might conduct $H^+$

rather than $Na^+$. More importantly, solid-state batteries with NaCMC and NaPAA binders did not function similarly to PVDF. This supports our conclusion that NaCMC might conduct $H^+$. Nevertheless, $Na^+$ conductivity cannot be ruled out in these compounds, particularly in the hydrated form, as hydration might facilitate the $Na^+$ hopping. Though it requires further investigation, the distance between two $Na^+$ is too large in these compounds for $Na^+$ to hop without the help of a hydrated solvent.

## Insight into the binding mechanism of ICIB

The binding mechanisms of ICIB are different from those of conventional PVDF, where binding is largely based on physical interactions.[33] We hypothesize that the binding ability of ICIB could be due to the condensation of its $OH^-$ groups with the surface functional groups of electrode materials and substrates. We dissolved ICIB in water and let the water evaporate at RT, intending to get free-standing films. However, free-standing films were not obtained. Instead, ICIB stuck strongly to the glass substrate (digital images are provided in Fig. S12†). This contrasts with PVDF and NaCMC, where free-standing films were obtained readily when NMP-PVDF and water-NaCMC solutions were dried. This experiment signals that the binding mechanisms of ICIB are different compared to conventional organic binders. And strong bonding to glass substrate suggests surface groups are vital to achieving binding with ICIB. The presence of $OH^-$ groups in ICIB can be observed from TG and FTIR (Fig. S5, S8b and S9b†). A total weight loss of 0.76%, 0.69%, and 0.15% was observed for SPP, SHMP, and STMP, respectively (Fig. 1d). A rather high weight loss of 4% was observed for SMS. This weight loss could be due to the loss of $OH^-$ in the form of $H_2O$. $LiH_2PO_4$ exhibited a weight loss of ~18% between 300 and 400 °C due to the formation of $LiPO_3$. The FTIR spectra of all binders show a peak between 2500–3500 $cm^{-1}$ (Fig. S5, S8b and S9b†). These peaks are assigned to $OH^-$ groups.[34] These $OH^-$ groups disappeared after drying at 100 °C (for SPP, SHMP, and STMP) at 300 °C (for SMS), which indicates that the $OH^-$ groups are condensable during the drying (Fig. S5 & S8b†). ICIB might hydrolyze further and produce more $OH^-$ groups when dissolved in water during the slurry-making process. These $OH^-$ groups will condense with the surface functional groups of electrode materials and provide binding during the drying process. In the absence of electrode material, two metaphosphate groups will condense. Therefore, it is vital to have surface functional groups on electrode materials to provide strong binding.

## Electrochemical performance of ICIB in sodium-ion batteries (SIBs)

The state of the binders within the composite electrodes is obviously amorphous. XRD patterns were collected on composite electrodes (NMO (80%) + (STMP or SHMP (10%)) + carbon (10%)) that were dried and heated at various temperatures [Fig. S6†]. The patterns of the electrodes did not show any pronounced reflections corresponding to binders. However, new unidentified reflections evolved after heating the electrodes at 600 °C, which might have originated due to the solid-state reactions between the electrode material and the phosphate binder. While the amorphous state for SHMP can be expected, the amorphous state of STMP in the electrode is rather surprising. The strong interactions between NMO and binder might have probably inhibited the crystallization of these binders.

The reversible capacities of hard carbon (HC) are 243 and 265, and 262 mA h $g^{-1}$ when cycled with PVDF, NaCMC, and NaALG, respectively (Fig. 2a). The reversible capacities of HC-SHMP and HC-MB (mixed binder-STMP-SPP) cells are 306 mA h $g^{-1}$ and 340 mA h $g^{-1}$. Interestingly, the reversible capacities of HC-STMP and HC-SPP alone are lower than that of HC-MB cells (Fig. 2b), which might be due to the synergistic effect of these binders. A reversible capacity of approximately 250 mA h $g^{-1}$ was reported for HC-CMC cells at 25 mA $g^{-1}$ by Dahbi *et al.*[8] A reversible capacity of ~300 mA h $g^{-1}$ and ~275 mA h $g^{-1}$ was obtained here when cycled at 20 mA $g^{-1}$ using HC-MB and HC-SHMP cells. The rate capability of the cells was improved further by adding additional conductive carbon in the electrode-making process. When additional carbon was added (10 wt%), the reversible capacity of HC-SHMP cells increased to ~360 mA h $g^{-1}$ (Fig. S16†). Further improvements in the rate capability of the HC electrodes are possible by inducing more functional groups on HC and enhancing the ionic conductivity of ICIB. The discharge profile of HC has two distinct regions – a sloping region between 2.0–0.1 V and a plateau-like region between 0.1–0.0 V. In our earlier studies on HC, the sloping region was designated for the adsorption of Na into defects followed by insertion into nano-sized graphitic layers, while the plateau-like region was affirmed to the pooling of Na into the nanopores formed by the random orientation of graphitic layers.[35,36] We also proposed that the capacity of the sloping region must be restricted to 93 mA h $g^{-1}$ ($Na_{24}C$), but the capacity in the plateau region can be modulated. Evidently, the discharge capacities of the sloping region were confined to <100 mA h $g^{-1}$ irrespective of binders, and capacities of the plateau region increased significantly when ICIB were used. A key to achieving high capacity in the plateau region is to reduce over-discharge potential. A low over-discharge potential result in a longer discharge plateau and increases the associated capacity. A high over-discharge potential leads to a fast reaching of 0.0 V and decreases the capacity in the plateau region. Discharging below 0.0 V will lead to deposition of Na–metal. HC–ICIB showed low over-discharge potential compared to HC-PVDF cells, confirming the improved interfacial resistance between ICIB and HC. A lower interfacial resistance was observed for HC-SHMP and HC-MB than with HC-PVDF cells. The IR of the HC-MB cell was ~660 Ω, while that of the HC-PVDF cell was ~1060 Ω (Fig. 2c). The reduced interfacial resistance signifies the facile charge transfer kinetics between HC and ICIB and

 

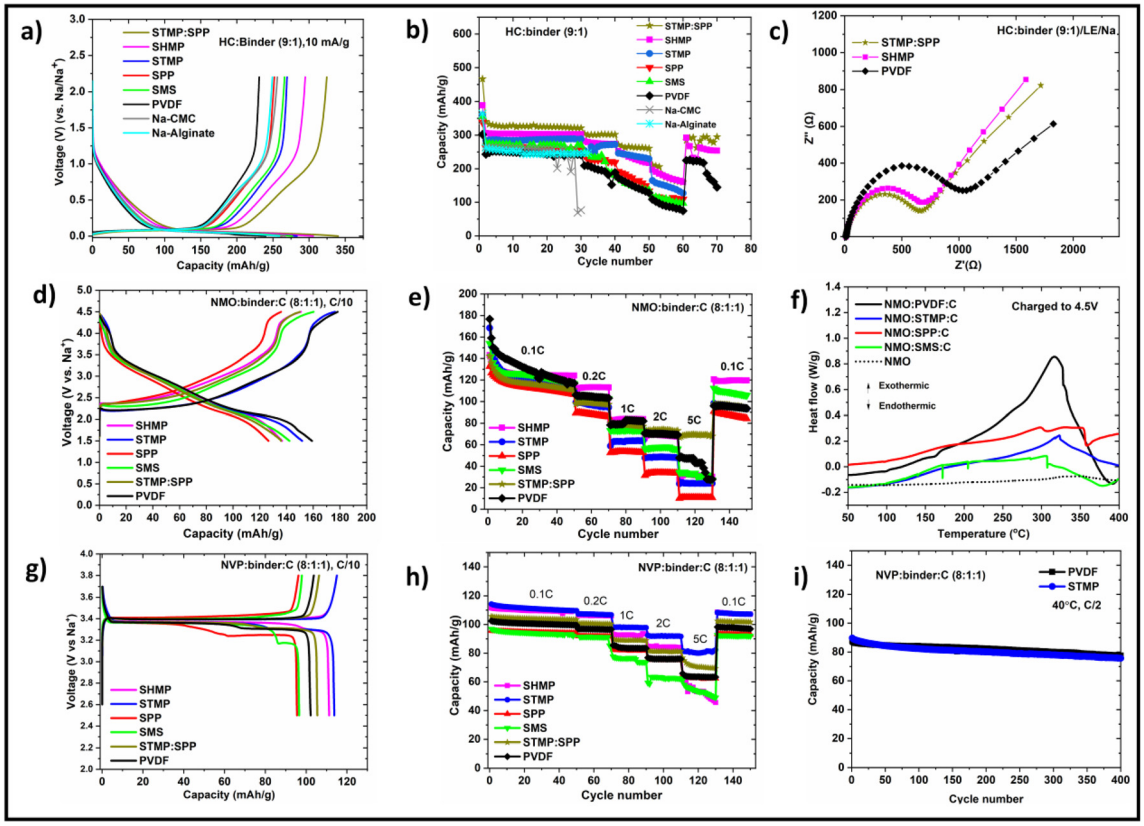


**Fig. 2** Electrochemical performance of ICIB in SIBs: (a) discharge–charge profiles of HC : binder (9 : 1) cells (second cycle) at 10 mA $g^{-1}$, (b) cyclic performance of the same cells cycled at different current rates and 25 °C, (c) Nyquist plot of HC-PVDF, HC-SHMP and HC-MB cells measured before cycling; (d) charge–discharge profiles of NMO : binder : C (8 : 1 : 1) cells obtained at a current rate of C/10 (second cycle), (e) cyclic performance of the same cells cycled at different current rates and 25 °C, (f) DSC of charged electrodes (NMO-PVDF, NMO-STMP, NMO-SPP, and NMO-SMS); for DSC measurements, electrodes were charged electrochemically until 4.5 V *vs.* $Na/Na^+$. The charged electrodes were first washed with DMC and dried (80 °C), and then the powder was scratched off from the current collector for DSC. (g) Charge–discharge profiles of NVP : binder : C (8 : 1 : 1) cells with different binders obtained at C/10 (second cycle); (h) cycling performance of the same cells cycled at different current rates and 25 °C, (i) cycling performance of NVP-PVDF, NVP-STMP cells cycled at 40 °C and C/2. The active material was 2.0 to 3.0 mg $cm^{-2,}$ and the thickness of the electrode was 40–50 μm. The thickness of the current collector and separator is 190 and 500 μm, respectively. Na–Metal thickness is 250 μm, and the diameter is 7 mm. Approximately 150 μL electrolyte was used for each cell. The C-rate was calculated assuming the following specific capacities for materials; NMO: 180 mA h $g^{-1}$, NVP: 117 mA h $g^{-1}$. Additional electrochemical data related to HC, NMO, and NVP electrodes are given in the ESI.† The comparison of the reversible capacities with all binders is given in Tables S2 and S3 of ESI.†

minimizes the over-discharge potential, leading to decreased polarization between the discharge–charge curves of HC. The polarization between discharge–charge curves was 27 mV for HC-MB and 33 mV for HC-PVDF. The high reversible capacity found for HC–ICIB cells reveals the inherent potential of HC and makes it potentially viable for commercialization. The better electrochemical properties of HC–ICIB cells compared to HC-PVDF cells could be due to the strong binding between HC and ICIB. HC might condense more intensely due to the presence of carboxyl and epoxy groups in addition to OH groups on the surface of the HC. Fig. S47† shows the XPS spectra of hard carbon. The peaks at 286 and 289 eV indicate the presence of oxygen originated from these functional groups. These carboxyl and epoxy groups will condense with the $OH^-$ groups of the binder and provide a strong binding between ICIB and HC. The low interfacial resistance of HC–ICIB cells could also be due to the strong binding between HC and ICIB.

$Na_{0.7}Mn_{0.9}Mg_{0.1}O_2$ (NMO)–ICIB cells displayed superior capacity retention compared to NMO-PVDF cells (Fig. 2e and Table S3†). The reversible capacity of the NMO-PVDF cell in the second cycle is 159 mA h $g^{-1}$, the highest among all binders (Fig. 2e and S18†). However, a drastic capacity fading was observed with cycling (94 mA h $g^{-1}$ after 150 cycles). The reversible capacity of the NMO-SHMP cell was 137 mA h $g^{-1}$ in the second cycle and reduced to 120 mA h $g^{-1}$ after 150 cycles. The capacity retention of the NMO-PVDF cell is 59%, while that of the NMO-SHMP cell is 87% over 150 cycles (Table S3†). Further, NMO-MB cells exhibited the highest rate capability among the investigated binders with a capacity of ~70 mA h $g^{-1}$, while all other cells show only half of this capacity at 5C (Fig. 2e). The reason for the lower rate capability of NMO–ICIB cells (except NMO-MB cell) than NMO-PVDF cells could be due to the low binding strength of ICIB towards NMO. In contrast to hard carbon, oxides will use surface $OH^-$ groups to con-

dense and bind. Therefore, the binding strength of oxides depends on the $OH^-$ groups present on the surface of NMO. FTIR shows no evidence of $OH^-$ groups. Due to the high-temperature synthesis (900 °C) and low surface area (1.6 $m^2$ $g^{-1}$) of NMO, we expect the number of $OH^-$ groups on the surface of NMO to be significantly less and eventually led to weak binding and lower rate capability. The rate capability of NMO could be improved significantly by inducing surface $OH^-$ groups on NMO. Besides cycling stability, another major concern with layered cathode materials is their low thermal stability in the charged state (Na is removed). P2-type layered cathode materials release oxygen in the highly charged state, destabilizing the structure and eventually leading to phase transformations at high temperatures with heat release. Controlling such heat evolution is essential to prevent thermal runaway in batteries. Interestingly, ICIB acts as a heat sink by absorbing the exothermic heat evolved from charged cathode materials at high temperatures. DSC of NMO-PVDF electrodes exhibited a strong exothermic peak centered at 316 °C (Fig. 2f). The exothermic heat associated with this transition was 428 J $g^{-1}$. In contrast, the exothermic heat released by NMO-SPP, NMO-STMP, and NMO-SMS electrodes was 302, 143, and 38 J $g^{-1}$, respectively. The higher heat release by NMO-SPP electrodes compared to NMO-STMP and NMO-SMS electrodes is related to the exothermic transition of SPP to STMP at 340 °C (Fig. 1e). This exothermic heat might have manifested in the heat evolution by NMO-SPP electrodes. Overall, the heat evolved from NMO–ICIB electrodes was low and insignificant in NMO-SMS electrodes. We postulate that even this little heat can be eliminated by employing optimized quantities of NMO and ICIB. This can have strong implications for preventing thermal runaways in batteries. The lesser heat evolved by NMO–ICIB electrodes than NMO-PVDF is attributed to the chemical reaction between ICIB and charged NMO cathodes, which could have minimized the net exothermic heat. It can also be related to the oxygen-scavenging act of ICIB.

All binders performed well with $Na_3V_2(PO_4)_3$ (NVP), but STMP stands out. A reversible capacity of 114 mA h $g^{-1}$ was observed for the NVP-STMP cell, a value close to the theoretical capacity of NVP (117 mA h $g^{-1}$) (Fig. 2g and S20†). A relatively low reversible capacity of 102 mA h $g^{-1}$ is observed for the NVP-PVDF cell. Comprehensively, all NVP cells maintained high-capacity retention (≥94%) (Fig. 2h and Table S3†). Long-term cycling measurements were performed on NMO and NVP at 40 °C (Fig. S21† and Fig. 2i). Fast capacity fading was observed for NMO probably due to the electrolyte decomposition, triggered by high cut-off voltage (4.5 V) and temperature. However, NVP delivered a stable capacity of 80 mA h $g^{-1}$ even after cycling at 40 °C for 400 cycles.

## Electrochemical performance of ICIB in lithium-ion batteries (LIBs)

The electrochemical performance of Li-based binders is shown in Fig. 3. $LiPO_3$ electrodes were derived from $LiH_2PO_4$ electrodes as $LiPO_3$ is not soluble in water. Initially, we made electrodes with $LiH_2PO_4$ and heated them at 120 °C and 320 °C in air. The electrodes heated at 320 °C are noted as $LiPO_3$ as $LiH_2PO_4$ loses water when heated beyond 300 °C according to TGA (Fig. S9†). The 2$^{nd}$ discharge capacities of G-PVDF, G-SHMP, G-LHPO, and G-LPO cells were 368, 390, 403, and 382 mA h $g^{-1}$, respectively. The reversible capacities of the cells after 30 cycles were 368, 383, 376, and 385 mA h $g^{-1}$, respectively. The reversible capacities are close to the theoretical specific capacity of graphite (372 mA h $g^{-1}$). The reversible capacity of G-PVDF cells at a 1C rate is 288 mA h $g^{-1}$. Whereas the reversible capacities of G-SHMP, G-LHPO, and G-LPO cells at 1C rate are 78, 144, and 22 mA h $g^{-1}$, respectively. Though the theoretical capacity was achieved with G-ICIB cells at a C/10 rate, the C-rate capability of G-ICIB cells is significantly lower. Interestingly all G-ICIB cells restored the theoretical capacity when cycled at low rates. In the case of HC, the reversible capacities of HC-PVDF, HC-SHMP, HC-LHPO, and HC-LPO cells are 268, 215, 301, and 259 mA h $g^{-1}$, respectively. The reversible capacities of HC at 60 mA $g^{-1}$ are 170, 132, 190, and 157 mA h $g^{-1}$ for HC-PVDF, HC-SHMP, HC-LHPO, and HC-LPO cells, respectively. LHPO is better for HC in LIBs. Hard carbon and graphite offer direct comparison as both are made of carbon. Hard carbon is built of nano graphitic domains arranged in a random card model.[37] Graphite is built of ordered graphene layers. HC was synthesized at 1200 °C and got a significant number of defects and contains various functional groups as proved by XPS (Fig. S47†). The average particle size is ~5 μm. Graphite was obtained commercially and used as received. The average particle size is ~3–5 μm. Graphitization occurs generally above 2000 °C, where any defect and functional groups will be removed. Therefore, graphite does not possess functional groups to condense with ICIB and eventually showed poor binding and rate capability. We suggest that by inducing the functional groups on graphite, the binding strength can be enhanced, and graphite's cycling and rate capability can be significantly improved. It should be mentioned that we were able to make hard carbon & NMO electrodes even with 5 wt% of ICIB. The electrochemical results are shown in Fig. S17 & S19.† Though we could make graphite electrodes using $LiH_2PO_4$ and $Li_2Si_5O_{11}$ as binders, our attempts to make electrodes using graphite and SHMP failed. Therefore, we have added 5 wt% of dopamine in the electrode-making process of graphite using SHMP as a binder. With the addition of tris buffer (10 mM, pH 8.5), dopamine will self-polymerize on the surface of graphite and facilitated coating with SHMP. Polydopamine was subsequently removed by heating the electrodes at 320 °C before cycling.

$Li_4Ti_5O_{12}$ (LTO) is another interesting material as an anode for LIBs. LTO-PVDF cells delivered the full theoretical specific capacity of 175 mA h $g^{-1}$ when cycled at a C/10 rate. However, LTO-ICIB cells showed less reversible capacity. The reversible capacities of LTO-LPO and LTO-SHMP are 147 and 154 mA h $g^{-1}$. We attribute this low capacity of LTO to its low binding strength towards SHMP and LPO. We treated LTO in 1 M

 

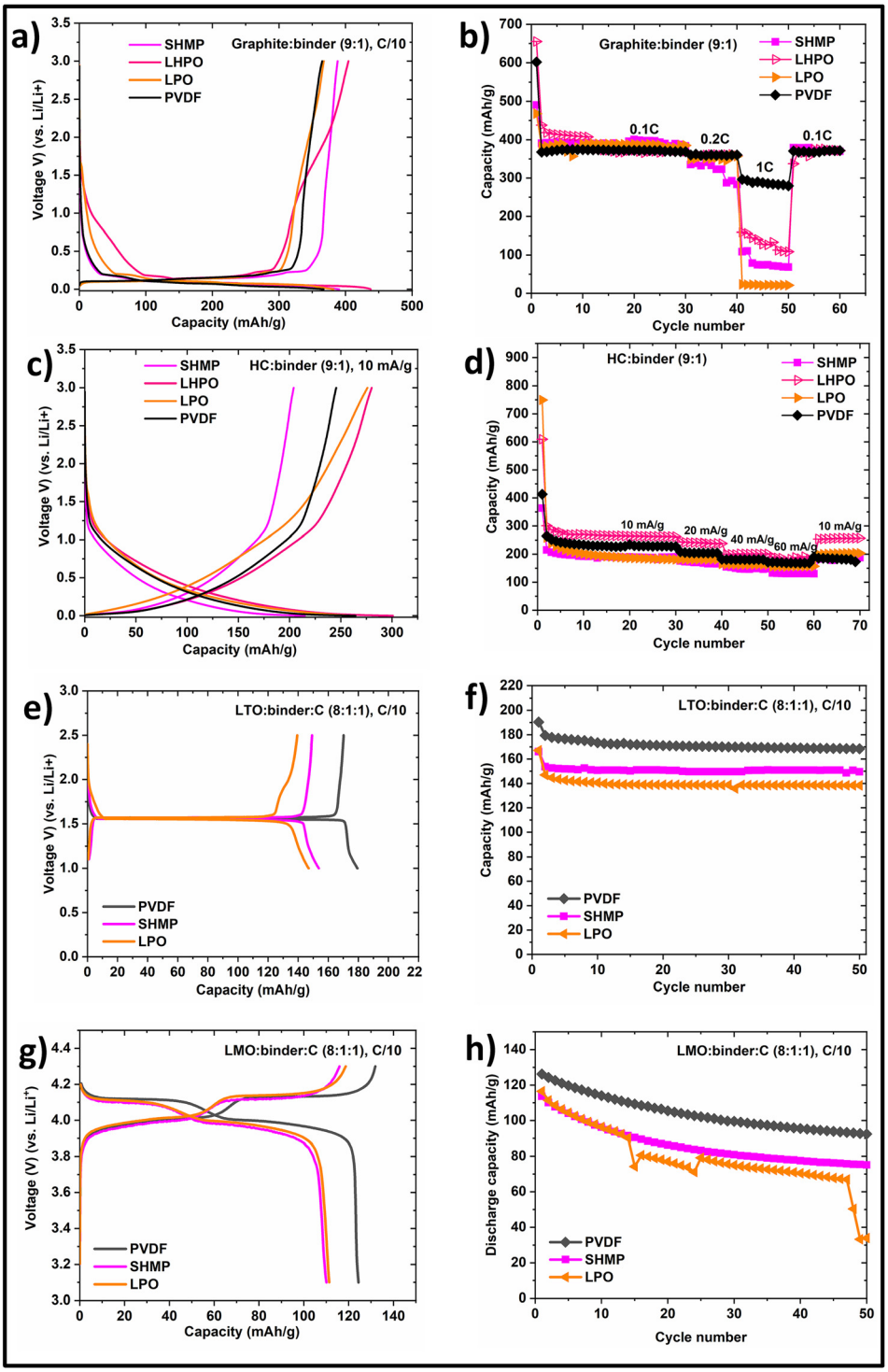


**Fig. 3** Electrochemical performance of the ICIB in LIBs. (a) Shows 2nd discharge–charge profiles of G-PVDF, G-SHMP, G-LPO, and G-LHPO cells; (b) cyclic performance of the same cells cycled at different current rates and 25 °C; (c) 2nd discharge–charge profiles of HC-PVDF, HC-SHMP, HC-LPO, HC-LHPO; (d) cyclic performance of the same cells cycled at different current rates and 25 °C; (e) 2nd discharge–charge profiles of LTO (f) their cycling performance; (g) 2nd charge–discharge profiles of LMO; (h) their cycling performance. The complete details of reversible capacities and capacity retentions for LIBs is given in Tables S4 & S5.† The active material was 2.0 to 3.0 mg $cm^{-2}$, and the thickness of the electrode was 40–50 μm. The thickness of the current collector and separator is 190 and 500 μm, respectively. Li–Metal thickness is 200 μm, and the diameter is 7 mm. Approximately 150 μL of electrolyte was used for each cell. The C-rate was calculated assuming the following specific capacities for materials; LMO: 148 mA h $g^{-1}$, LTO: 175 mA h $g^{-1}$, graphite: 372 mA h $g^{-1}$.

$HNO_3$ to induce surface $OH^-$ groups. But it led to $Li^+$ exchange with $H^+$. Fig. S48† shows the XRD and FTIR patterns of pure LTO and $HNO_3$ treated LTO. No $OH^-$ groups are evident from the pure LTO, but a strong peak was seen between 3000–3500 $cm^{-1}$, which signifies the presence of $OH^-$ groups. But in the XRD of $HNO_3$ treated LTO, significant changes can be seen which could be due to $Li^+$ exchange with $H^+$. We have also tested $LiMn_2O_4$ (LMO) against ICIB. LMO-PVDF cell delivers a theoretical specific capacity (148 mA h $g^{-1}$) in its first charge but fades with cycling. The capacity of LMO-LPO and LMO-SHMP cells also faded with cycling, but the initial capacity is 105 and 110 mA h $g^{-1}$, respectively. We are trying to coat these electrode materials with $SiO_2$, which can generate a significant amount of $OH^-$ groups on the surface, resulting in better binding and might improve the electrochemical performance.

## ICIBs for solid-state batteries (SSBs)

SSBs potentially offer higher energy density and safety than conventional non-aqueous batteries. However, the manufacturing of SSBs is challenging owing to the mechanical rigidity of solid electrolytes (SEs). Two methodologies were adopted in the literature to fabricate SSBs. The first approach involves co-sintering SEs with cathode layers (CLs), then pressing them with metal electrodes.[38,39] In this process, a significant fraction of SEs (30–40 wt%) needs to be mixed with cathode material to provide adequate ionic wiring in the cathode layer. This fraction of SE in the cathode layer is electrochemically inactive and reduces the energy density of SSBs. Besides, controlling the volume changes in such SSBs is difficult owing to the mechanical rigidity of SEs. Volume changes can lead to the isolation of electrode particles, loss of interfacial contact, blocking of ion transport (within cathode layer, across the cathode layer, and SE), and eventually lead to capacity fading. Such problems are trivial in batteries with LEs as volume changes can be accommodated in electrode materials. In the second and broadly adapted approach, cathode layers were coated on pre-sintered SE discs using organic binders; and subsequently, cathode layers were wetted with LEs to induce ionic transport.[40] SSBs fabricated *via* the second approach work well. However, such SSBs are not fundamentally different from non-aqueous batteries (considering the flammability and low thermal stability of LEs, and organic binders). On the other hand, wetting with LEs is necessary to enable ionic transport. But ICIB, with their unique ionic conducting and binding properties, enabled the flexible processing and functioning of SSBs without conceding their attributes.

To test this hypothesis, SSBs using PVDF and ICIB were fabricated. Sodium beta alumina (SBA) discs were employed as SEs due to their high ionic conductivity ($1.4 \times 10^{-3}$ S $cm^{-1}$) at RT. In type I SSB, NMO was coated as a cathode layer on SBA discs using a PVDF binder. SSB was made by pressing Na–metal as an anode to the other side of the SBA disc (Na/SBA/NMO-PVDF-C). The Nyquist plot of the Na/SBA/NMO-PVDF-C cell consists of a depressed semicircle with resistance over 400 kΩ (Fig. 4a). The Na/SBA/NMO-PVDF-C cell did not exhibit sig-

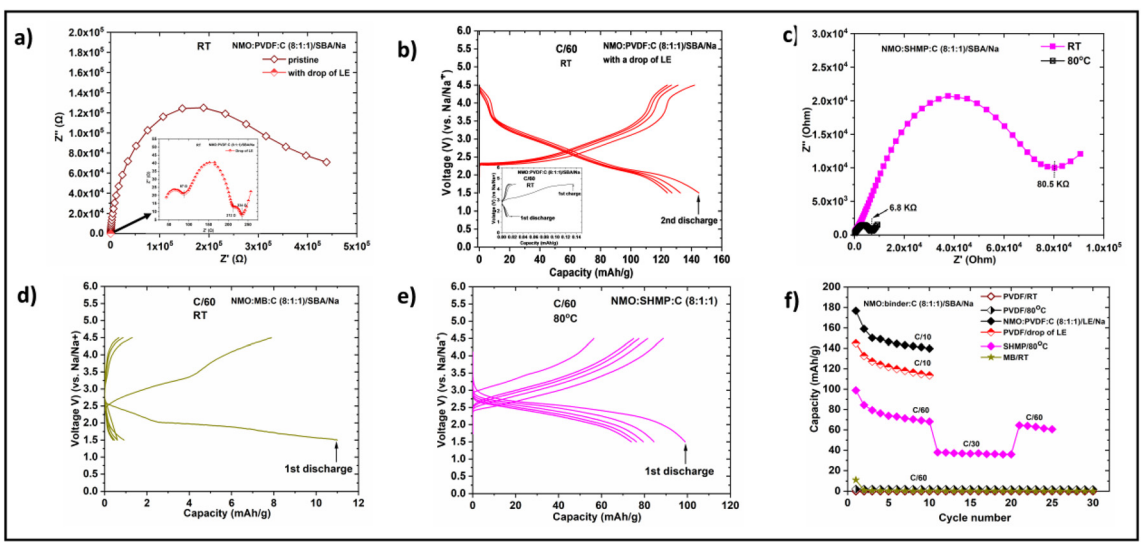


**Fig. 4** Electrochemical performance of ICIB in SSBs. (a) Nyquist plot of Na/SBA/NMO-PVDF-C cell recorded at RT and inset shows the Nyquist plot of the same cell recorded after adding a drop of liquid electrolyte (LE) to the cathode layer; (b) charge–discharge profiles of the Na/SBA/NMO-PVDF-C cell obtained after adding a drop of LE to CL (Na/SBA/NMO-PVDF-C-LE). Inset shows charge–discharge cycles without LE. (c) Nyquist plot of Na/SBA/NMO-SHMP-C cell obtained at RT and 80 °C; (d) charge–discharge profiles of the Na/SBA/NMO-MB-C cell obtained at RT; (e) charge–discharge profiles of Na/SBA/NMO-SHMP-C cell obtained at 80 °C. (f) Cycling performance of Na/SBA/NMO-PVDF-C (obtained RT and 80 °C), Na/SBA/NMO-PVDF-C-LE cells (the cycling was also compared with pure liquid electrolyte cell Na/LE/NMO-PVDF-C) Na/SBA/NMO-MB-C at RT and compared with Na/SBA/NMO-SHMP-C at 80 °C.

 

nificant capacity when cycled (Fig. 4b inset). The cell was dismantled in a glove box, and a drop of LE was added to the cathode layer (Na/SBA/NMO-PVDF-C-LE). The Nyquist plot of this cell consists of two well-defined semicircles with a total resistance of 234 Ω (magnified in the inset of Fig. 4a). The first semicircle (87 Ω) signifies the interfacial resistance between SBA and Na–metal. Although the Na–metal layer was not wetted, the LE dropped on the cathode layer could diffuse across the SE disc and wet the interface between Na–metal and SBA. The interfacial resistance of the second semicircle was 212 Ω. The addition of LE induces ionic conductivity within the cathode layer, across the cathode layer, and SBA, and this notably reduced the resistance of the cathode layer. The Na/SBA/NMO-PVDF-C-LE cell is performed typically as the cell with pure LE (Na/LE/NMO-PVDF-C) (Fig. 4b and f). These studies emphasize that the addition of LE is obligatory for the operation of SSBs with a PVDF binder.

In type II SSB, NMO was coated on SBA using SHMP. After coating the CL, the SBA discs were heated at 300 °C. Na-Metal was pressed onto the other side of these discs to complete the fabrication of SSB (Na/SBA/NMO-SHMP-C). The Nyquist plot of the Na/SBA/NMO-SHMP-C cell consists of one depressed semicircle with a total resistance of 80.5 kΩ. The resistance dropped to 6.8 kΩ when the temperature of the cell was raised to 80 °C. In contrast to the cell with PVDF (Na/SBA/NMO-PVDF-C), this cell could be cycled at 80 °C. The first charge and discharge capacities of Na/SBA/NMO-SHMP-C cells were 56 and 99 mA h $g^{-1}$, respectively. However, the capacity faded gradually, and a capacity of 68 mA h $g^{-1}$ was obtained after 10 cycles. This low discharge capacity could be due to the large IR observed for Na/SBA/NMO-SHMP-C cells. The total resistance of pure SSB at 80 °C was ~29 times higher than that of SSB wetted with LE. The high interfacial resistance limits the ion transport across the interface and results in low capacity. The reason for high interfacial resistance could be due to the low ionic conductivity ($2.5 \times 10^{-9}$ S $cm^{-1}$) of SHMP at 80 °C and the modified surface of SBA during NMO coating with SHMP. The coating of NMO using SHMP exposes the SBA discs to water, which would have modified the surface of SBA. Coating of NMO using PVDF uses NMP solvent, which is stable against SBA. Capacity fading could also be due to the increased interfacial resistance between Na and SBA during cycling (Fig. S25†). Interfacial resistance increased to ~198 kΩ after 10 cycles and ~3.8 MΩ after 25 cycles. Overall, the electrochemical performance of the SSBs with ICIB is not appealing due to the low IC of SHMP and high interfacial resistance between Na–metal and SBA. Nevertheless, ICIB paved an untrodden path for the flexible processing and operation of SSBs without LEs. We postulate that by using ICIB with higher ionic conductivities and water-stable SEs, high-performance, sustainable and safe SSBs can be realized.

Since the organic binders showed ionic conductivity similar to ICIB, we fabricated SSBs with NaCMC and NaPAA. SSBs with these binders should work if the ionic conductivity of these binders is due to $Na^+$ and not $H^+$. The EIS and electrochemical results are summarized in Fig. S26 and Table S6.† These cells performed like a cell with PVDF. They did not function either at RT or 80 °C. But they worked well when liquid electrolyte was added. These results further emphasize the importance of intrinsic ionic conductivity in binders.

## Outlook

In this report, we revealed the potential of inorganic binders in electrochemical energy storage and demonstrated the importance of having intrinsic ionic conductivity in binders. Beyond ionic conductivity, binding properties, and excellent thermal stability, ICIB can absorb the heat evolved by charged cathodes, which will significantly enhance the thermal stability of batteries. The binding ability of ICIB could be due to the condensation of its $OH^-$ groups with the surface functional groups of electrode materials and substrates. Therefore, the binding properties of ICIB can be improved and tailored by inducing surface functionalities on electrode materials and by optimizing the processing conditions such as pH of the binder solutions, amount of binder, binder to water ratio, and drying conditions. Our experiments inferred that ICIB has good adhesion towards the glass (which could be due to the surface $OH^-$ groups). Therefore, we suggest that coating electrode materials with $SiO_2$ might significantly improve the adhesion, thereby electrochemical properties. Further, the rate capability of electrodes can be improved by enhancing the ionic conductivity of ICIB. The binding properties combined with intrinsic ionic conductivity provide unique opportunities in solid-state batteries. As far as SSB applications are concerned, the ionic conductivity of ICIB needs to be improved. The ionic conductivities of ICIB reported here are in the range of $5 \times 10^{-10}$ to $5 \times 10^{-11}$ S $cm^{-1}$ at 60 °C, which are low. However, the ionic conductivities of these ICIB could be significantly improved by doping with aliovalent cations, and there is a scope for identifying new inorganic binders with high ionic conductivity. As ICIBs are emission-free and do not require organic solvents for processing, battery manufacturing and recycling will get cheaper and greener.

## Author contributions

MAR conceived the idea of ICIBs based on his preliminary experiments. The work was supervised by MAR with the assistance of MF. Full experimental work and figure preparation was done by ST & VP. All the experiments related to anode, IC & SSB were performed by ST. VP performed all the experiments relevant to cathodes. Experiments related to binder characterization, large area fabrication, morphological investigations & figure preparations were carried out both by ST & VP. MAR analyzed the results and wrote the full manuscript in discussions with ST, VP & MF.

## Conflicts of interest

The authors declare no competing financial interests.

## Acknowledgements

This work contributes to the research performed at CELEST (Center for Electrochemical Energy Storage Ulm-Karlsruhe) and was funded by the German Research Foundation (DFG) under project ID 390874152 (POLiS Cluster of Excellence, EXC 2154). MAR acknowledges Engineering and Physical Sciences Research Council (EPSRC): grant – EP/V014994/1. The authors acknowledge the help of Mr Mervyn Soans for providing LMO & LTO active materials and Mr Yanlei Xiu for DSC measurements. MAR acknowledges Dr Aulice Scibioh for correcting and proofreading the draft.

## Notes and references

1 H. Chen, M. Ling, L. Hencz, H. Y. Ling, G. Li, Z. Lin, *et al.*, Exploring Chemical, Mechanical, and Electrical Functionalities of Binders for Advanced Energy-Storage Devices, *Chem. Rev.*, 2018, **118**(18), 8936–8982.

2 D. Song, X. Wang, E. Zhou, P. Hou, F. Guo and L. Zhang, Recovery and heat treatment of the $Li(Ni_{1/3}Co_{1/3}Mn_{1/3})O_2$ cathode scrap material for lithium ion battery, *J. Power Sources*, 2013, 232.

3 X. Zhang, Q. Xue, L. Li, E. Fan, F. Wu and R. Chen, Sustainable Recycling and Regeneration of Cathode Scraps from Industrial Production of Lithium-Ion Batteries, *ACS Sustainable Chem. Eng.*, 2016, **4**(12), 7041–7049.

4 W. Zhu, D. R. Schmehl, C. A. Mullin and J. L. Frazier, Four common pesticides, their mixtures and a formulation solvent in the hive environment have high oral toxicity to honey bee larvae, *PLoS One*, 2014, **9**(1), e77547.

5 D. E. Malek, L. A. Malley, T. W. Slone, G. S. Elliott, G. L. Kennedy, W. Mellert, *et al.*, Repeated dose toxicity study (28 days) in rats and mice with N- methylpyrrolidone (NMP), *Drug Chem. Toxicol.*, 1997, **20**(1–2), 63–77.

6 D. L. Wood, J. D. Quass, J. Li, S. Ahmed, D. Ventola and C. Daniel, Technical and economic analysis of solvent-based lithium-ion electrode drying with water and NMP, *Drying Technol.*, 2018, **36**(2), 234–244.

7 J. Ordoñez, E. J. Gago and A. Girard, Processes and technologies for the recycling and recovery of spent lithium-ion batteries, *Renewable Sustainable Energy Rev.*, 2016, 60.

8 M. Dahbi, T. Nakano, N. Yabuuchi, T. Ishikawa, K. Kubota, M. Fukunishi, *et al.* Sodium carboxymethyl cellulose as a potential binder for hard-carbon negative electrodes in sodium-ion batteries, *Electrochem. Commun.*, 2014, **44**, 66–69.

9 K. C. Kil and U. Paik, Lithium salt of carboxymethyl cellulose as an aqueous binder for thick graphite electrode in lithium ion batteries, *Macromol. Res.*, 2015, **23**(8), 719–725.

10 J. H. Lee, U. Paik, V. A. Hackley and Y. M. Choi, Effect of Carboxymethyl Cellulose on Aqueous Processing of Natural Graphite Negative Electrodes and their Electrochemical Performance for Lithium Batteries, *J. Electrochem. Soc.*, 2005, **152**(9), A1763–A1769.

11 S. Hidayat, T. Cahyono, J. Y. Mindara, N. Riveli, W. Alamsyah and I. Rahayu, The optimization of CMC concentration as graphite binder on the anode of $LiFePO_4$ battery, *IOP Conf. Ser.: Mater. Sci. Eng.*, 2017, **196**, 012035.

12 M. Armand, P. Axmann, D. Bresser, M. Copley, K. Edström, C. Ekberg, *et al.*, Lithium-ion batteries – Current state of the art and anticipated developments, *J. Power Sources*, 2020, **479**, 228708.

13 Y. Orikasa, Y. Gogyo, H. Yamashige, M. Katayama, K. Chen, T. Mori, *et al.* Ionic Conduction in Lithium Ion Battery Composite Electrode Governs Cross-sectional Reaction Distribution, *Sci. Rep.*, 2016, **6**(1), 26382.

14 V. A. Nguyen and C. Kuss, Review—Conducting Polymer-Based Binders for Lithium-Ion Batteries and Beyond, *J. Electrochem. Soc.*, 2020, **167**(6), 065501.

15 M. D. Bhatt and J. Y. Lee, High capacity conversion anodes in Li-ion batteries: A review, *Int. J. Hydrogen Energy*, 2019, **44**(21), 10852–10905.

16 L. Qiu, Z. Shao, M. Yang, W. Wang, F. Wang, J. Wan, *et al.*, Study on effects of carboxymethyl cellulose lithium (CMC-Li) synthesis and electrospinning on high-rate lithium ion batteries, *Cellulose*, 2014, **21**(1), 615–626.

17 L. Qiu, Z. Shao, D. Wang, W. Wang, F. Wang and J. Wang, Enhanced electrochemical properties of $LiFePO_4$ (LFP) cathode using the carboxymethyl cellulose lithium (CMC-Li) as novel binder in lithium-ion battery, *Carbohydr. Polym.*, 2014, **111**, 588–591.

18 N. P. W. Pieczonka, V. Borgel, B. Ziv, N. Leifer, V. Dargel, D. Aurbach, *et al.*, Lithium Polyacrylate (LiPAA) as an Advanced Binder and a Passivating Agent for High-Voltage Li-Ion Batteries, *Adv. Energy Mater.*, 2015, **5**(23), 1501008.

19 M. Rani, S. Rudhziah, A. Ahmad and N. Mohamed, Biopolymer Electrolyte Based on Derivatives of Cellulose from Kenaf Bast Fiber, *Polymers*, 2014, **6**(9), 2371–2385.

20 A. S. Samsudin, W. M. Khairul and M. I. N. Isa, Characterization on the potential of carboxy methyl-cellulose for application as proton conducting biopolymer electrolytes, *J. Non-Cryst. Solids*, 2012, **358**(8), 1104–1112.

21 Y. Zhao, Z. Liang, Y. Kang, Y. Zhou, Y. Li, X. He, *et al.*, Rational design of functional binder systems for high-energy lithium-based rechargeable batteries, *Energy Storage Mater.*, 2021, 35.

22 D. G. Fauteux and J. Shi, Lithium ion electrolytic cell and method for fabricating same, *Japan: United States Patent*, 5856045, 1999.

23 A. Kay, Inorganic binders for battery electrodes and aqueous processing thereof, *United States: United States*, PCT/IB09/52543, 2011.

24 C. Wei and M. N. Obrovac, Inorganic Compounds as Binders for Si-Alloy Anodes, *J. Electrochem. Soc.*, 2021, **168**(2), 020505.

25 H. M. Ondik, The structure of anhydrous sodium trimetaphosphate $Na_3P_3O_9$, and the monohydrate, $Na_3P_3O_9.H_2O$, *Acta Crystallogr.*, 1965, **18**(2), 226.

26 M. Ezzaafrani, A. Ennaciri, M. Harcharras, R. Khaoulaf and F. Capitelli, Crystal structure and infrared spectrum of new

 

magnesium tetra-ammonium cyclotriphosphate tetrahydrate $Mg(NH_4)_4(P_3O_9)_2{\cdot}4H_2O$, *Z. Kristallogr.*, 2012, **227**(3), 141–146.

27 H. Ettis, H. Naïli and T. Mhiri, Synthesis and Crystal Structure of a New Potassium–Gadolinium Cyclotetraphosphate, $KGdP_4O_{12}$, *Cryst. Growth Des.*, 2003, **3**(4), 599–602.

28 T. Glonek, Did Cyclic Metaphosphates Have a Role in the Origin of Life?, *Origins Life Evol. Biospheres*, 2021, **51**(1), 1–60.

29 M. Sharma and S. Yashonath, Correlation between conductivity or diffusivity and activation energy in amorphous solids, *J. Chem. Phys.*, 2008, **129**(14), 144103.

30 M. L. F. Nascimento, E. do Nascimento and S. Watanabe, Test of Anderson-Stuart model and the "universal" conductivity in rubidium and cesium silicate glasses, *Braz. J. Phys.*, 2005, **35**(3a), 626–631.

31 O. L. Anderson and D. A. Stuart, Calculation of Activation Energy of Ionic Conductivity in Silica Glasses by Classical Methods, *J. Am. Ceram. Soc.*, 1954, **37**(12), 573–580.

32 B. Viswanathan and M. Helen, Is_Nafion_R_the_only_Choice, *Bull. Catal. Soc. India*, 2007, **6**, 50–66.

33 X. Zhong, J. Han, L. Chen, W. Liu, F. Jiao, H. Zhu, *et al.*, Binding mechanisms of PVDF in lithium ion batteries, *Appl. Surf. Sci.*, 2021, **553**, 149564.

34 W. Zuo, X. Liu, J. Qiu, D. Zhang, Z. Xiao, J. Xie, *et al.*, Engineering $Na^+$-layer spacings to stabilize Mn-based layered cathodes for sodium-ion batteries, *Nat. Commun.*, 2021, **12**(1), 4903.

35 M. Anji Reddy, M. Helen, A. Groß, M. Fichtner and H. Euchner, Insight into Sodium Insertion and the Storage Mechanism in Hard Carbon, *ACS Energy Lett.*, 2018, **3**(12), 2851–2857.

36 H. Euchner, B. P. Vinayan, M. A. Reddy, M. Fichtner and A. Groß, Alkali metal insertion into hard carbon – the full picture, *J. Mater. Chem. A*, 2020, **8**(28), 14205–14213.

37 D. A. Stevens and J. R. Dahn, High Capacity Anode Materials for Rechargeable Sodium-Ion Batteries, *J. Electrochem. Soc.*, 2000, **147**(4), 1271–1273.

38 Q. Ma, C. L. Tsai, X. K. Wei, M. Heggen, F. Tietz and J. T. S. Irvine, Room temperature demonstration of a sodium superionic conductor with grain conductivity in excess of 0.01 S $cm^{-1}$ and its primary applications in symmetric battery cells, *J. Mater. Chem. A*, 2019, **7**(13), 7766–7776.

39 P. Xu, W. Rheinheimer, S. N. Shuvo, Z. Qi, O. Levit, H. Wang, *et al.*, Origin of High Interfacial Resistances in Solid–State Batteries: Interdiffusion and Amorphous Film Formation in $Li_{0.33}La_{0.57}TiO_3/LiMn_2O_4$ Half Cells, *ChemElectroChem*, 2019, **6**(17), 4576–4584.

40 X. Han, Y. Gong, K. Fu, X. He, G. T. Hitz, J. Dai, *et al.*, Negating interfacial impedance in garnet-based solid-state Li metal batteries, *Nat. Mater.*, 2017, **16**(5), 572–579.